Implementation of a 1 G Star-Mesh Graphene Quantized Hall Array Resistance Standard Network for High Resistance Calibration

Implementation of a 1 GΩ Star-Mesh Graphene Quantized Hall Array Resistance Standard Network for High Resistance Calibration

Marta Musso, Wei-Chen Lin, Yanfei Yang, Ngoc Thanh Mai Tran, Alireza R. Panna, Cheng-Hsueh Yang, Randolph E. Elmquist, *Senior Member, IEEE*, David B. Newell, Chi-Te Liang, Massimo Ortolano, Albert F. Rigosi, *Member, IEEE*, and Dean G. Jarrett, *Fellow, IEEE*

***Abstract*—A 1 GΩ star-mesh quantized Hall array resistance standard (QHARS) assembled from 37 individual elements, each exhibiting the quantum Hall effect (QHE), was fabricated and tested. The 1 GΩ QHARS has three orders of magnitude fewer elements than a largely series 1 GΩ QHARS, which would require approximately 77480 elements. A dual source bridge (DSB), using a nanovolt detector and a modified algorithm using least-squares analysis was used to interpolate a bridge null from five measurement points taken near the null of the linear measurement system. The 1 GΩ star-mesh QHARS was used as a standard to calibrate 100 MΩ, 1 GΩ, and 10 GΩ high resistance standards. The star-mesh measurements agreed within the combined standard uncertainties of the values of these standards based on traditional high resistance scaling from the $i = 2$ quantized Hall resistance value of 12906.4037...Ω, where guarded Hamon transfer standards and DSBs are used to build-up to high resistance ranges from 1 MΩ standard resistors.**

***Index Terms*—Bridge circuits, calibration, electrical resistance measurement, graphene, Hall effect devices, resistance, standards.**

I. Introduction

THE highly favorable electrical properties of graphene have made it the focus of many research pursuits during the past decade or so [1], [2], [3], [4]. When grown epitaxially on 4H-SiC, graphene exhibits a robust quantum Hall effect (QHE) across a wide range of magnetic fields (B-fields) and thus may be conveniently employed into devices for electrical metrology. For these devices to be successfully implemented as standards, the measured resistance must be well quantized [5], [6], [7], [8], [9], [10]. Most epitaxial graphene (EG)-based devices that are used as resistance standards operate at the resistance plateau formed by the QHE at the Landau level $\nu = 2$ ($R_H = h/(\nu e^2) \approx$ 12906.4037 Ω) [11], [12], [13], [14].

Historically, this single value of quantized resistance has constrained the extent to which one may disseminate the unit of ohm. Efforts to expand the access to other quantized values include two main endeavors: 1) using quantized Hall array resistance standards (QHARSs) to link elements in parallel, series [15], [16], [17], [18], [19], [20], [21], [22], [23], or in more general topologies [24], [25] or 2) using p-n junctions [26], [27], [28], [29], [30]. Both approaches enable access to resistances $R = qR_H$, q being a positive rational number, but with the former endeavor being reported more frequently in the scope of metrological objectives. For high resistance values, $q \gg 1$, requiring a large number of devices.

Despite the more frequent usage of EG devices in recent times, a limitation to QHARS fabrication is the total area of high-quality EG, which is currently grown at the centimeter scale [31]. This restriction translates to a very approximate quantized resistance upper bound of 6.5 MΩ (assuming 500 elements in series), which is much smaller than the range of resistances calibrated globally, with some requiring PΩ levels [32].

Transcending this constraint relies on the application of the wye-delta (Y–Δ) star-mesh transformations, an approach that can scale up to high enough values that one meets the limit of meaningful quantized resistances [23], [33], [34], [35], [36]. By utilizing a star-mesh QHARS device designed with the guidance of the mathematical framework presented in [33], a 1 GΩ device is shown in this work to be used as a reference standard for high resistance. The device was tested in conjunction with a new configuration of the NIST dual source bridge (DSB). This combination of quantized device and resistance bridge is a strong potential candidate for replacing the traceability chain for resistances of the same order of

Received 31 March 2025; revised 24 May 2025; accepted 9 June 2025. Date of publication 20 June 2025; date of current version 24 July 2025. This work was supported by the Ministero dell'Università e della Ricerca (MUR) Progetti di Ricerca di Rilevante Interesse Nazionale (PRIN) Bando 2020 through the Project CAPSTAN Quantum Electrical Italian National Capacitance Standard under Grant 2020A2M33J. The Associate Editor coordinating the review process was Dr. Helko E. van den Brom. *(Corresponding author: Marta Musso.)*

Marta Musso is with the Department of Electronics and Telecommunications, Politecnico di Torino (POLITO), 10129 Turin, Italy, and also with the National Institute of Standards and Technology (NIST), Gaithersburg, MD 20899 USA (e-mail: marta.musso@polito.it).

Wei-Chen Lin is with NIST, Gaithersburg, MD 20899 USA, also with the Department of Engineering and System Science, National Tsing Hua University, Hsinchu 300044, Taiwan, and also with Academia Sinica, Taipei 115029, Taiwan.

Yanfei Yang, Alireza R. Panna, Randolph E. Elmquist, David B. Newell, Albert F. Rigosi, and Dean G. Jarrett are with NIST, Gaithersburg, MD 20899 USA.

Ngoc Thanh Mai Tran is with NIST, Gaithersburg, MD 20899 USA, and also with the Joint Quantum Institute, University of Maryland, College Park, MD 20742 USA.

Cheng-Hsueh Yang and Chi-Te Liang are with the Graduate Institute of Applied Physics, National Taiwan University, Taipei 10617, Taiwan.

Massimo Ortolano is with the Department of Electronics and Telecommunications, Politecnico di Torino (POLITO), 10129 Turin, Italy.

Digital Object Identifier 10.1109/TIM.2025.3581627

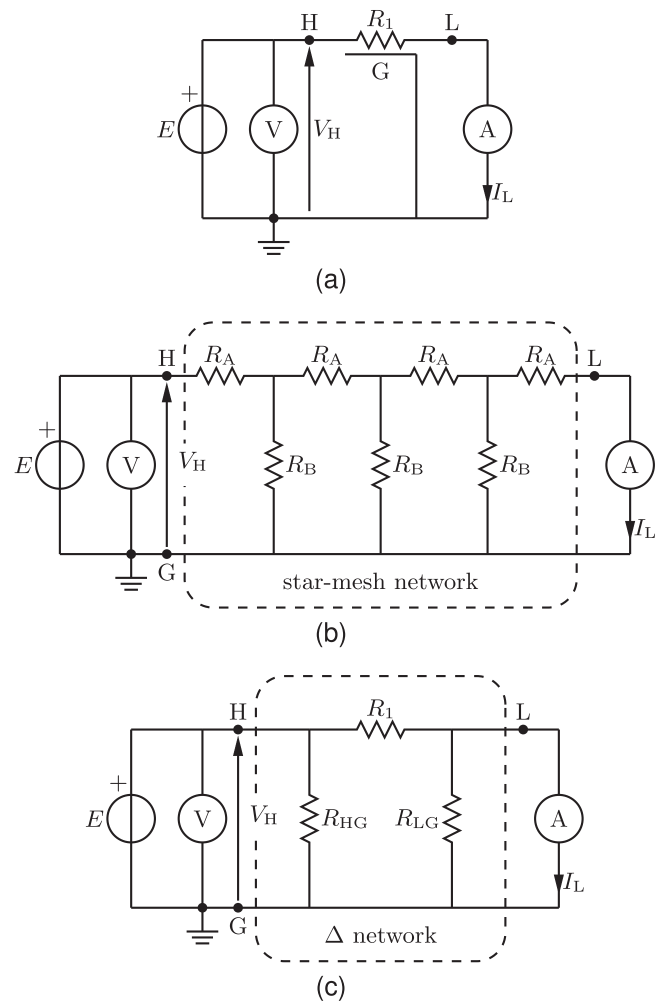

Fig. 1. (a) Measurement schematic for the definition of a three-terminal resistance: R_1 is the measurand resistance with high potential terminal H, low potential terminal L, and the ground terminal G; E is a voltage source; the voltmeter measures the voltage V_H across H and ground and the ammeter measures the current I_L flowing out of L. (b) Three-terminal resistance definition applied to a star-mesh resistance network composed of the series resistances R_A and the parallel resistances R_B. (c) Δ network equivalent to the one in (b).

magnitude as the device output. Furthermore, replacing such long traceability chains (i.e., those requiring several steps to scale up from a single quantized Hall resistance standard) will enable future improvement on precision measurements for higher resistance ranges.

II. Star-Mesh Resistance Network

A. Theory

In this work, resistances are defined as three-terminal standards [37], according to the schematic of Fig. 1(a). The measurand resistance is

$$R_1 = \left.\frac{V_H}{I_L}\right|_{V_L=0}, \tag{1}$$

where V_H is the voltage at the high potential terminal H, I_L is the current flowing out of the low terminal L, and V_L is the voltage at L.

High resistance standards have been implemented in [32], [34], [38], [39], and [40] as Y networks of low resistance elements to improve temperature and humidity stability. Cascading Y networks allows the implementation of *star-mesh* networks.[1] An example of the latter with series resistances R_A and parallel resistances R_B is shown in Fig. 1(b). This can be generally represented by the Δ equivalent network of Fig. 1(c) [42], where the values of R_1, R_{HG}, and R_{LG} can be computed, for example, by iterated Y–Δ transformations [34], [39] (alternative methods of analysis can be found in [43], [44], and [45]). In this Δ equivalent network, owing to the three-terminal resistance definition, the measured resistance coincides with R_1 and the stray resistances R_{HG} and R_{LG} do not affect the measurement.

In a QHARS, R_A and R_B are composed of interconnected elements, each exhibiting the same quantized resistance R_H. As a consequence, $R_1 = qR_H$, where, in general, q is a positive rational number. In order to obtain high resistance values, it is convenient to maximize R_A and minimize R_B. For this reason, this work considers networks in which R_A is composed of elements in series, numbering a, such that $R_A = aR_H$, and R_B is composed of b parallel QHE elements, $R_B = R_H/b$. This choice yields an integer q, minimizing the number of elements at the expense of the possibility of closely approximating a specific resistance value (e.g., decadal values commonly employed in calibrations). To design a star-mesh QHARS with a specific value of q, minimizing the number of elements, one may use the general optimization process described in [33], involving recursive star-mesh transformations. This process, at the level of recursion M, generates a network with an approximate total number of elements given by

$$D_T(M, b, q) = \frac{2^M}{b}(bq+1)^{2^{-M}} - \frac{2^M}{b} + \left(2^M - 1\right)b \tag{2}$$

and with

$$a \approx \frac{1}{b}(bq+1)^{2^{-M}} - \frac{1}{b}. \tag{3}$$

For the optimization, one finds from (2) values of M and b yielding a suitable number $D_T(M, b, q)$ and from (3) determines a.

A possible solution for a target resistance of 1 GΩ at the level of recursion $M = 2$ is $b = 3$, $a = 7$, and $D_T = 37$. In this arrangement, the elements of the Δ equivalent circuit have values $R_1 = 84847R_H \approx 1.095069$ Ω and $R_{LG} = R_{HG} = (7 + 23/72)R_H \approx 94.46770$ Ω.

B. 1 GΩ Graphene QHARS

The device design followed the configuration proposed in Section II-A, according to the simplified schematic of Fig. 1(b). R_A is composed of seven series-connected elements and R_B is composed of three parallel-connected elements.

The QHARS device was prepared with a procedure similar to that described in [23], [46], and [47]. The graphene monolayer is epitaxially grown on a 4H-SiC substrate and the

[1] In this work, the term *star-mesh resistance network* denotes a network of resistances whose three-terminal equivalent resistance can be computed by means of recursive star-mesh transformations [38], [41]; in circuit theory, these are more commonly indicated with the term *ladder networks*.

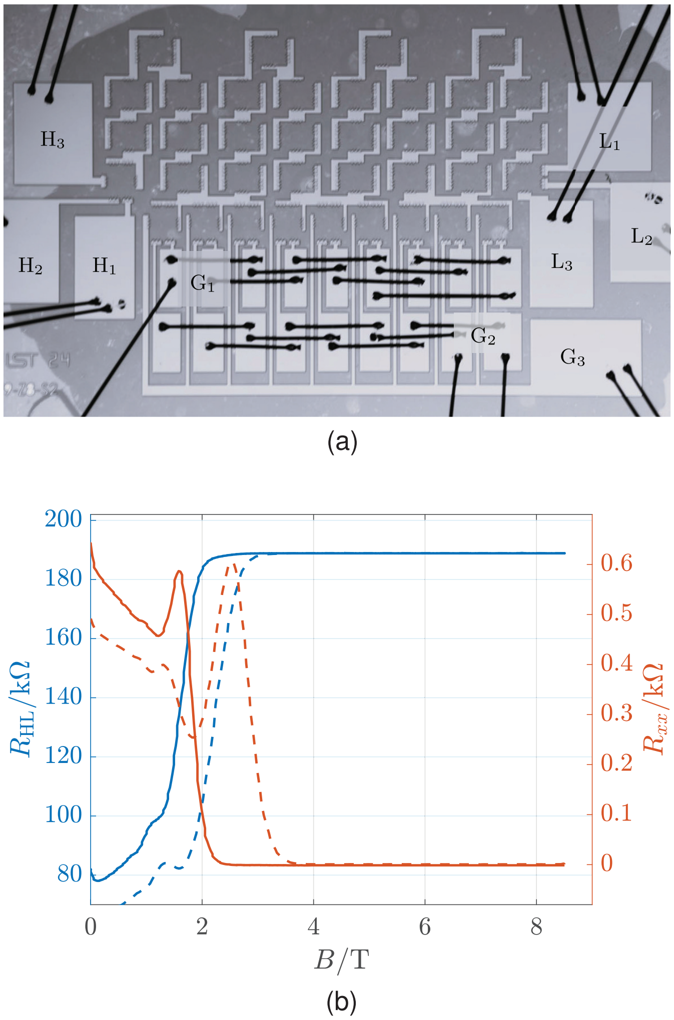

Fig. 2. 1 GΩ device employed in this experiment. (a) Optical image of the 1 GΩ device with the wire bonds at the terminals G_1 and G_2 to implement the triple series connection. (b) Magneto-transport measurements of this star-mesh QHARS before (solid line) and after (dashed line) annealing to increase the carrier density [52].

monolayer quality is inspected using optical and confocal laser scanning microscopy [48]. Then, a lithographic process is used to fabricate the QHE elements, contacts, and superconducting NbTiN interconnections [31], [49]. The use of superconducting material enables crossover-free interconnections [31] throughout the device, except at the terminal elements, where crossovers are required to facilitate triple connections to a measuring system [15], [50].

The QHARS device fabrication process and graphene growth are described in more detail in our recent articles [23], [47], [51]. The individual QHE elements size is 300μm × 300μm the resulting chip size is approximately 5mm × 3mm.

A photograph of the device is presented in Fig. 2(a). The device has terminals H_1–H_3, G_1–G_3, and L_1–L_3. These allow the interconnection of the QHARS to an external circuit by means of triple connections to minimize the error introduced by the wiring resistances [15]. The QHARS device is mounted onto a transistor outline (TO-8) package.

Fig. 2(b) reports the magnetotransport measurements of the QHARS, obtained by ramping B from zero to 8.5 T at around a temperature of 3 K. The blue curves in Fig. 2(b) represent the resistance $R_{\mathrm{HL}} = R_1 \parallel (R_{\mathrm{HG}}+R_{\mathrm{LG}})$, where $\parallel$ denotes the parallel equivalent resistance, obtained by disconnecting terminals G_1, G_2, and G_3 from ground. When the device is fully quantized, $R_{\mathrm{HL}} \approx 188.9$ kΩ. This resistance was measured by injecting a 1 μA current through the terminals H_3 and L_3 with a source-measure unit (Keithley 2612A) and by measuring the voltage across the H_2 and the L_2 terminals with a digital multimeter (Keysight 3458A).

The longitudinal resistance R_{xx} of a single element was also measured, shown in the plot with orange curves. This resistance was measured by injecting a 1 μA current through the terminals H_3 and L_3 and by measuring the voltage across H_2 and H_1.

The solid lines represent data taken at a carrier density at which most of the measurements presented in this article were conducted: the QHARS is n-type doped and the carrier density is $n_e \approx 1.4 \times 10^{11}$ cm^{-2}, estimated from the magneto-transport measurement. The dashed lines correspond instead to data collected after having annealed the device, thus increasing the carrier density [52]. In fact, the critical current I_C at which the QHE breaks down [53], [54], [55] depends on the carrier density and, for a single device, it has typical values in the range of a hundred μA [7], [19], [22], [54]. For the QHARS, the current through the devices connected to the H node is about V_1/R_A. This is the maximum current in the QHARS and should be less than the critical current I_C. As a consequence, the maximum applicable $V_1 \approx I_C R_A$ is of the order of 10 V for these conditions.

III. Dual Source Bridge

The DSB is used as the primary measurement technique for the high resistance values at NIST and other national metrology institutes because of its high accuracy and stability [8], [56], [57], [58]. The bridge was adapted from the Wheatstone bridge, employing the automated high resistance bridge method that was first proposed by Henderson [59]. A DSB is a voltage ratio bridge where the two resistors in the main arms of the Wheatstone bridge are replaced by two voltage sources. A simplified schematic of the bridge is illustrated in Fig. 3(a). The voltage sources V_1 and V_2 are two calibrators (Fluke 5730A and 5720A). The sources were calibrated using an automated potentiometer (Measurements International 8000A/8001A) based on a Cutkosky binary voltage divider [60], [61]. The detector D is a 7.5 digit digital nanovoltmeter (Keysight 34420A). The low sides of the two calibrators and the detector are connected to ground.

The measurement sequence can be summarized as follows.

1) The two calibrators are set to zero, $V_1 = V_2 = 0$ V.
2) The bridge offset is determined from a sequence of detector readings.
3) The calibrator voltage V_1 is set to establish the operating current; the calibrator voltage V_2 is stepped around the value $V_2 = -V_1 R_2^{\mathrm{ref}}/R_1^{\mathrm{ref}}$, where R_1^{ref} and R_2^{ref} are the reference values for the standards, in a 1%–10% range. A waiting time is added after each voltage adjustment to let the system reach a steady state.

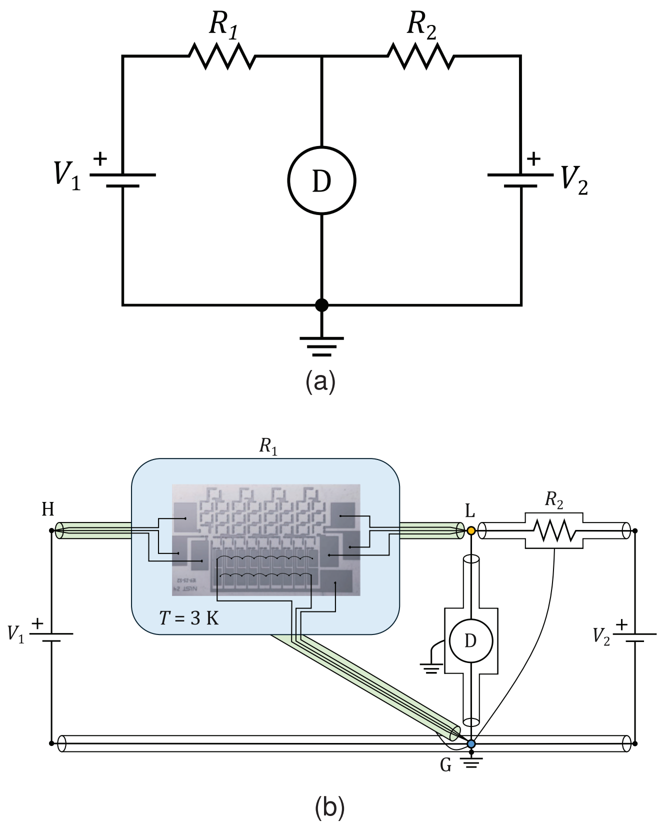

Fig. 3. (a) Principle schematic of the DSB. R_2 is the measurand resistance and R_1 is the calibrated resistance standard. V_1 and V_2 are the output voltages of two voltage calibrators. D is a voltage or current detector. (b) DSB measurement set-up. R_1 is the QHARS device in the cryostat, represented by the light blue rectangle. The ground star point is represented at node G (blue dot) and the detection point is represented at node L (yellow dot).

4) For each voltage V_2, the bridge response is determined from a sequence of detector readings.
5) Steps 1)–4) are repeated by reversing the polarity of the applied voltages.
6) For repeatability, steps 1)–5) are iterated to record a sequence of repeated measurements.
7) The unknown resistance R_2 is determined by least-squares regression according to the measurement model derived in Section IV.

A Visual Basic program was developed to control the bridge, carrying out the sequence of measurement steps automatically.

To confirm the bridge operation and performance before measuring a graphene QHARS, a prototype $1\,\mathrm{G}\Omega$ room-temperature star-mesh resistance network was compared against a $1\,\mathrm{G}\Omega$ calibrated resistance standard. The prototype has the same configuration of the QHARS described in Section II and the measurements were performed at several voltages from 10 V to 50 V. Fig. 4(a) shows a picture of the prototype inside its box. This was assembled by combining commercial precision resistors and trimmers to have R_A and R_B [see Fig. 1(b)] as close as possible to the quantized values in the QHARS. The results from the prototype measurements are shown in Fig. 4(b) (the uncertainty bars in the figure represent the standard deviations of the measurements).

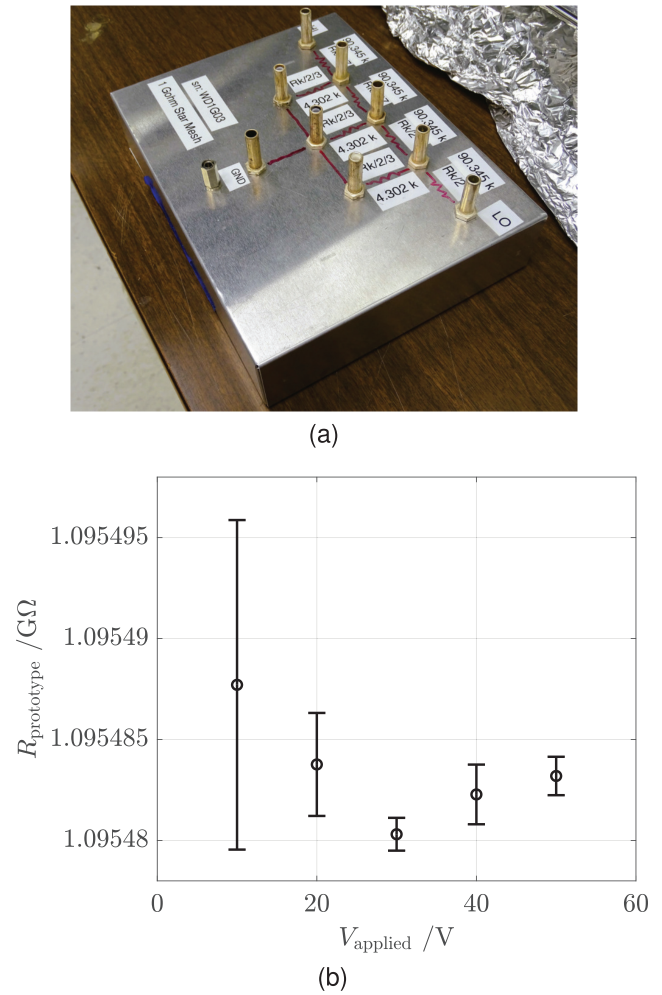

Fig. 4. (a) Picture of the $1\,\mathrm{G}\Omega$ prototype star-mesh network with the same configuration of the QHARS described in Section II. (b) DSB measurement of the prototype star-mesh network against a $1\,\mathrm{G}\Omega$ calibrated standard resistor.

The DSB measurements with the QHARS were conducted with the QHARS stored in a wet cryostat, maintained at a base temperature of approximately 3 K and a magnetic field of 8.5 T in persistent mode. The three resistance standards under calibration, with nominal values of 100 MΩ, 1 GΩ, and 10 GΩ, were housed in a temperature-controlled air bath set to 23 °C.

Fig. 3(b) shows an illustrative schematic of the bridge setup, along with the QHARS and the measured resistor. The triple connection to the graphene QHARS is highlighted in the schematic. A junction box was constructed to concentrate all connections to the ground, minimizing interconnection resistances and preventing ground loops. This ground junction box is located in the schematic at node G (blue dot). An additional junction box is inserted at node L (yellow dot) and the H node the three leads join directly at the V_1 calibrator output in a connector. Leads and resistors are shielded to reduce electrical noise.

IV. Measurement Model

The simplest measurement model can be derived from the circuit of Fig. 5, where R_1 is assumed to be a calibrated

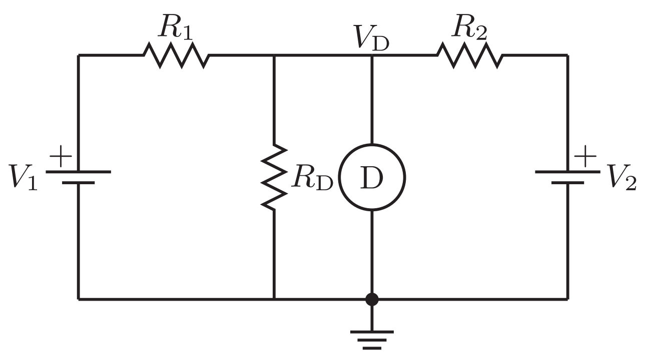

Fig. 5. Equivalent DSB circuit diagram for measurement model. D is a voltage or current detector and V_D is the voltage across it. R_D is the equivalent stray resistance in parallel with the detector.

resistance standard, R_2 is an unknown resistance standard, R_D is the equivalent stray resistance in parallel with the detector, V_1 is set to fix the measurement current, and V_2 is adjusted to find the value V_2^{NULL} for which the bridge is balanced with $V_D = 0$.

Using Millman's theorem [62], the detector voltage can be expressed as

$$V_D = \frac{V_1/R_1 + V_2/R_2}{1/R_1 + 1/R_2 + 1/R_D} \tag{4}$$

from which the unknown resistance can be determined as

$$R_2 = -\frac{V_2^{\mathrm{NULL}}}{V_1} R_1. \tag{5}$$

The detector voltage (4) can be rewritten as

$$V_D = V_{D0} + S V_2 \tag{6}$$

where

$$S = \frac{1/R_2}{1/R_1 + 1/R_2 + 1/R_D} \tag{7}$$

is the slope (sensitivity) coefficient and

$$V_{D0} = \frac{V_1/R_1}{1/R_1 + 1/R_2 + 1/R_D} \tag{8}$$

is the intercept term. These two parameters can be estimated by linear regression from a sequence of V_D measurements obtained at different values of V_2, from which $V_2^{\mathrm{NULL}} = -V_{D0}/S$.

Following the procedure described in Section III, the details of the algorithm are as follows. The resistance R_2 is measured N repeated times, and in the following, the data associated with each repetition are labeled with the subscript l, $l = 1, \dots, N$. The lth measurement consists of the following steps.

1) Both calibrators are set to zero to determine the offset and M detector readings $V_{D,jl}^{\mathrm{OS},+}$, $j = 1, \dots, M$, are recorded.
2) V_1 is set to a positive value V_1^+. Accordingly, V_2 is successively set to $2K+1$ voltages $V_{2,k}^+ = V_{2,0}^+ + (k/K)\Delta V_2$, $k = -K, \dots, K$. The center value $V_{2,0}^+$ is chosen from the nominal value R_2^{nom} of R_2 as $V_{2,0}^+ = R_2^{\mathrm{nom}} V_1^+ / R_1$ and ΔV_2 is a fixed maximum increment chosen to avoid overranging the detector. For each voltage pair V_1^+, $V_{2,k}^+$, M detector readings $V_{D,jkl}^{\mathrm{READ},+}$ are recorded.
3) Step 1 is repeated obtaining the readings $V_{D,jl}^{\mathrm{OS},-}$.
4) Step 2 is repeated reversing the polarity of both calibrators. For each voltage pair V_1^-, $V_{2,k}^-$, the detector readings $V_{D,jkl}^{\mathrm{READ},-}$ are recorded.

The above recorded data are averaged as $\bar{V}_{D,l}^{\mathrm{OS},\pm} = (1/M)\sum_{j=1}^{M} V_{D,jl}^{\mathrm{OS},\pm}$ and $\bar{V}_{D,kl}^{\mathrm{READ},\pm} = (1/M)\sum_{j=1}^{M} V_{D,jkl}^{\mathrm{READ},\pm}$ and the offset is removed as $\bar{V}_{D,kl}^{\pm} = \bar{V}_{D,kl}^{\mathrm{READ},\pm} - \bar{V}_{D,l}^{\mathrm{OS},\pm}$. To these averages, one can associate the type A uncertainties $u(\bar{V}_{D,l}^{\mathrm{OS},\pm})$, $u(\bar{V}_{D,kl}^{\mathrm{READ},\pm})$ and $u(\bar{V}_{D,kl}^{\pm})$, computed according to the *Guide to the Expression of Uncertainty in Measurement* (GUM) [63].

From (6), the above quantities are related by

$$\bar{V}_{D,kl}^{\pm} = V_{D0,l}^{\pm} + S_l^{\pm} V_{2,k}^{\pm} \tag{9}$$

where $S_l^{\pm}$ and $V_{D0,l}^{\pm}$ are the parameters that best approximate the data for a given polarity and l. This set of $2K+1$ equations can be put into the matrix form

$$\boldsymbol{V_D}_l^{\pm} = \boldsymbol{A}^{\pm} \boldsymbol{x}_l^{\pm} \tag{10}$$

where $\boldsymbol{x}_l^{\pm} = [V_{D0,l}^{\pm}, S_l^{\pm}]^{\top}$ (where $\top$ denotes the matrix transpose)

$$\boldsymbol{A}^{\pm} = \begin{bmatrix} 1 & V_{2,-K}^{\pm} \\ \vdots & \vdots \\ 1 & V_{2,K}^{\pm} \end{bmatrix} \tag{11}$$

is a $(2K+1) \times 2$ matrix and

$$\boldsymbol{V_D}_l^{\pm} = \begin{bmatrix} \bar{V}_{D,-Kl}^{\pm} \\ \vdots \\ \bar{V}_{D,Kl}^{\pm} \end{bmatrix}. \tag{12}$$

Since the vectors $\boldsymbol{V_D}_l^{\pm}$ have estimated covariance matrices $\boldsymbol{\Sigma}_l^{\pm} = \mathrm{cov}(\boldsymbol{V_D}_l^{\pm})$ equal to

$$\boldsymbol{\Sigma}_l^{\pm} = \begin{bmatrix} u^2\left(\bar{V}_{D,-Kl}^{\pm}\right) & 0 & \cdots & 0 \\ 0 & u^2\left(\bar{V}_{D,(-K+1)l}^{\pm}\right) & \cdots & 0 \\ \vdots & \vdots & \ddots & \vdots \\ 0 & 0 & \cdots & u^2\left(\bar{V}_{D,Kl}^{\pm}\right) \end{bmatrix} \tag{13}$$

and the matrices $\boldsymbol{A}^{\pm}$ have full-column rank, the set of equations (10) can be uniquely solved in the *generalized least squares* sense with the Gauss-Markov estimator [64, Sec. 4.2], and the solutions $\boldsymbol{x}_l^{\pm}$ are described as follows:

$$\boldsymbol{x}_l^{\pm} = \left(\boldsymbol{A}_l^{\pm\top} \left(\boldsymbol{\Sigma}_l^{\pm}\right)^{-1} \boldsymbol{A}_l^{\pm}\right)^{-1} \boldsymbol{A}_l^{\pm\top} \left(\boldsymbol{\Sigma}_l^{\pm}\right)^{-1} \boldsymbol{V_D}_l^{\pm}. \tag{14}$$

The covariance matrices of the solutions $\boldsymbol{x}_l^{\pm}$ are

$$\boldsymbol{\Sigma}_{\boldsymbol{x},l}^{\pm} = \mathrm{cov}\left(\boldsymbol{x}_l^{\pm}\right) = \hat{\sigma}_l^2 \left(\boldsymbol{A}_l^{\pm\top} \left(\boldsymbol{\Sigma}_l^{\pm}\right)^{-1} \boldsymbol{A}_l^{\pm}\right)^{-1}, \tag{15}$$

where $\hat{\sigma}_l^2$ is estimated by

$$\hat{\sigma_l}^2 = \frac{\left(\boldsymbol{V_D}_l^{\pm} - \boldsymbol{A}_l^{\pm}\boldsymbol{x}_l^{\pm}\right)^{\top} \left(\boldsymbol{\Sigma}_l^{\pm}\right)^{-1} \left(\boldsymbol{V_D}_l^{\pm} - \boldsymbol{A}_l^{\pm}\boldsymbol{x}_l^{\pm}\right)}{2K-1}. \tag{16}$$

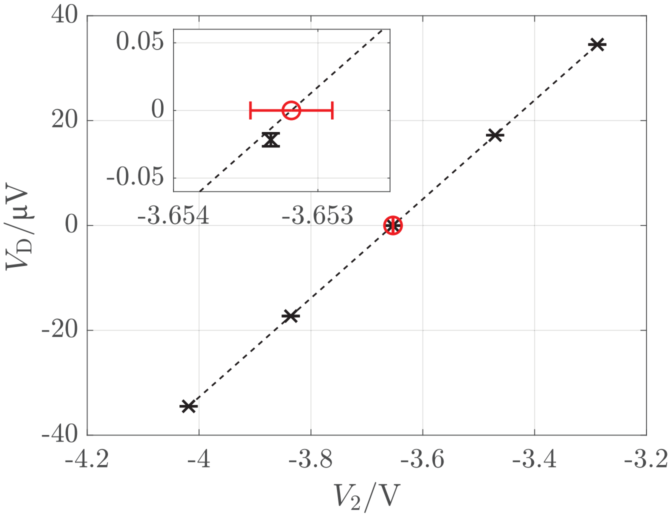

Fig. 6. Example of the method. The black crosses are $[\bar{V}^{+}_{D,-21}, \ldots, \bar{V}^{+}_{D,21}]$ as a function of $[V^{+}_{2,-2}, \ldots, V^{+}_{2,2}]$. The black dashed line is the linear fit. The red circle is $V_{2,1}^{\mathrm{NULL},+}$.

The interpolated balance values of V_2 are

$$V_{2,l}^{\mathrm{NULL},\pm} = -\frac{V^{\pm}_{\mathrm{D0},l}}{S^{\pm}_{l}}. \tag{17}$$

An example obtained for $l = 1$, $K = 2$, and $V_1 = 2$ V is shown in Fig. 6.

Using (5), the estimated values of R_2 are

$$R^{\pm}_{2,l} = -\frac{V_{2,l}^{\mathrm{NULL},\pm} - \Delta V_2^{\pm}}{V_1^{\pm} - \Delta V_1^{\pm}} R_1, \tag{18}$$

where $\Delta V_1^{\pm}$ and $\Delta V_2^{\pm}$ are the error terms associated with the calibrators, as discussed in Section V-B. The two polarities are averaged to obtain $R_{2,l}$.

The final result $\bar{R}_2$ is the weighted average of $R_{2,1}, \ldots, R_{2,N}$

$$\bar{R}_2 = \frac{\sum_{l=1}^{N} R_{2,l}/u\left(R_{2,l}\right)^2}{\sum_{l=1}^{N} 1/u\left(R_{2,l}\right)^2}. \tag{19}$$

The uncertainties $u(R_{2,l})$ and $u(\bar{R}_2)$ are evaluated according to the GUM [63] and GUM supplement 2 [65] starting from $\boldsymbol{\Sigma}^{\pm}_{\boldsymbol{x},l}$, $\Delta V_1^{\pm}$ and $\Delta V_2^{\pm}$.

In this work, all the above calculations and the propagation of uncertainty were performed with the help of the MATLAB library METAS UncLib [66].

V. Error Sources Analysis

A complete schematic of the DSB circuit is shown in Fig. 7, where the Δ equivalent circuit of the QHARS is shown. The purpose of this section is to describe which nonidealities of the implemented system can affect the measurement function (19) derived in Section IV, leading to a relative deviation of the measured value $\delta R_2 = (\bar{R}_2 - R_2)/R_2$. Some of these nonidealities are added in the schematic of Fig. 7: R_{ID} represents the input resistance of the detector; R_{O1} represents the output resistance of the calibrator generating V_1 and the contact resistance toward the node H where the triple connection

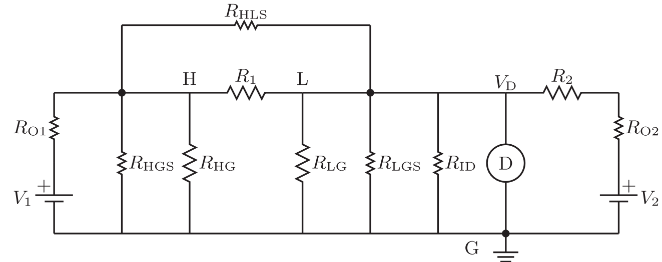

Fig. 7. Equivalent DSB circuit diagram: R_1, R_{HG}, and R_{LG} represent the elements of the equivalent Δ configuration of the QHARS; R_{ID} represents the input resistance of the detector; R_{O1}, and R_{O2} represent the output resistances of the voltage calibrators; R_{HLS}, R_{HGS}, and R_{LGS} represent the stray resistances of the cryostat and cabling. The stray resistors are drawn with smaller size.

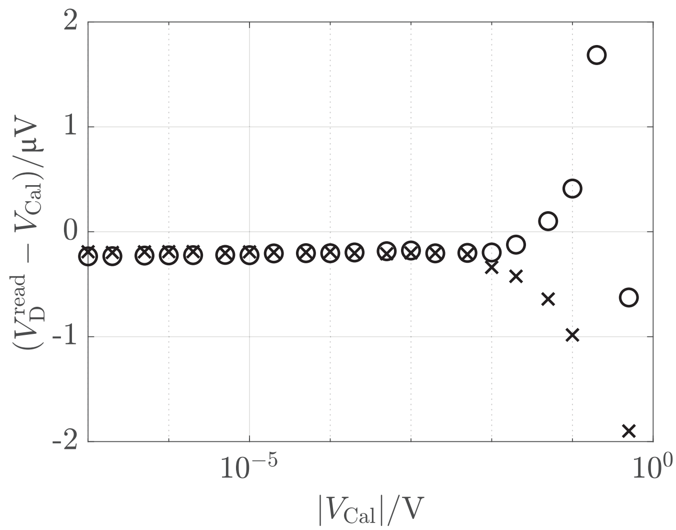

Fig. 8. Study on the linearity of the nanovoltmeter. The vertical scale represents the deviation of the nanovoltmeter reading $V_{\mathrm{D}}^{\mathrm{read}}$ with respect to the calibrator output voltage V_{Cal}, as a function of V_{Cal}, from ± 100 nV to ± 0.5 V. The circles represent the results for positive V_{Cal}, while the crosses represent the results for negative V_{Cal}.

joins; R_{O2} represents the output resistance of the calibrator generating V_2 and the contact and lead resistances of the connections to R_2; and R_{HLS}, R_{HGS}, and R_{LGS} represent the stray (leakage) resistances of the cabling.

A. Detector Error

Since the measurement model described in Section IV is based on a linear interpolation of the zero with offset compensation, the gain and offset errors of the detector are not relevant, but the measuring system needs to be linear. To test the linearity of the nanovoltmeter, the instrument was connected directly to the output of a calibrator, and the calibrator output voltage V_{Cal} was stepped from 100 nV to 0.5 V in a 1–2–5 progression for both polarities. Fig. 8 shows the deviation between the measured voltage $V_{\mathrm{D}}^{\mathrm{read}}$ and V_{Cal}. The results indicate that the nanovoltmeter is linear up to about ± 10 mV because the deviation below this limit is virtually constant, for both positive and negative values of the applied voltages.

The detector input resistance R_{ID} is in parallel to R_{LG} and R_{LGS} such that R_{D} in Fig. 5 and in (4) is $R_{\mathrm{D}} = R_{\mathrm{ID}} \parallel$

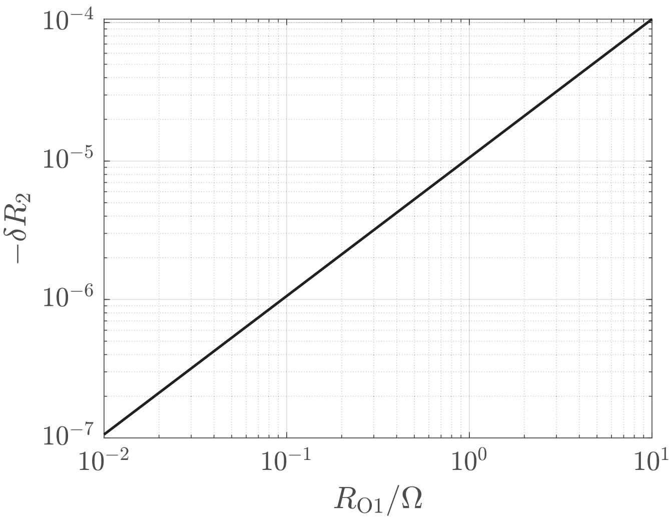

Fig. 9. Analysis of the effect of the calibrator output resistance R_{O1} on the measured resistance $\bar{R}_2$ performed with a Spice model built to mimic the behavior of R_1 in the quantized state.

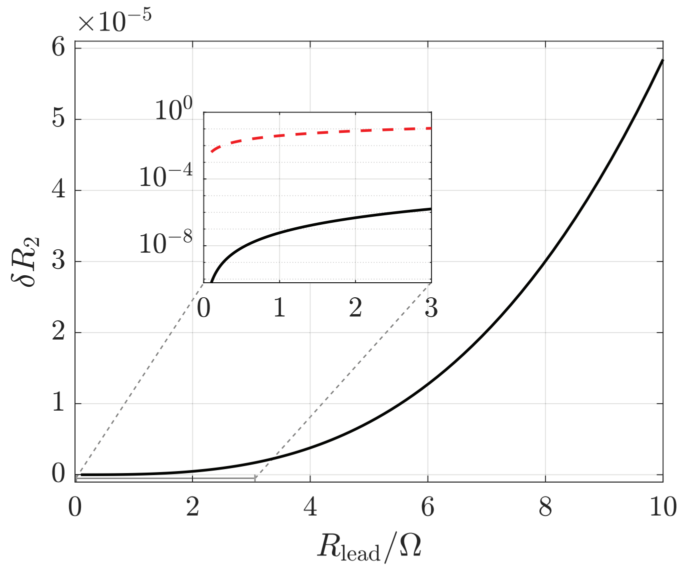

Fig. 10. Analysis of the effect of wires on the measured resistance $\bar{R}_2$ performed with a Spice model built to mimic the behavior of R_1 in the quantized state. R_{lead} is the resistance of each wire connecting the metal pads of the device to the ground located in the air bath outside the cryostat. The black solid line represents a device connected with a triple connection. In the inset, the same line is represented with a vertical logarithmic scale. In addition, the red dashed curve represents a device connected with the three leads in parallel, without taking advantage of the reduction in the contribution of R_{lead} obtained through the triple connection.

$R_{LG} \parallel R_{LGS} \approx R_{LG}$. From (4) and (5), this resistance does not cause any systematic error but decreases the bridge sensitivity coefficient S of the bridge.

The detector bias current and the detector offset are compensated by the zero readings and by the polarity reversals described in Section IV.

B. Calibrators

The calibrator errors are taken into account by the terms $\Delta V_1^{\pm}$ and $\Delta V_2^{\pm}$ in (18). These terms are assumed to have zero values with uncertainties $u(\Delta V_1^{\pm})$ and $u(\Delta V_2^{\pm})$ estimated from the calibrators specifications [67], [68]. Since the voltage settings $V_{2,k}^{\pm}$ are in the same calibrator range for any k, $u(\Delta V_2^{\pm})$ does not depend on k.

From Fig. 7, it can be proved that the resistance R_{O1} causes a relative deviation $\delta R_2 \approx -R_{O1}/(R_1 \parallel R_{HG}) \approx (10\ \mu\Omega/\Omega)(R_{O1}/\Omega)$ of the measured resistance $\bar{R}_2$ with respect to R_2, as shown in Fig. 9. To prevent this contribution from being significant, the three leads of the triple connection are joined in a connector directly at the output of the calibrator, yielding a value of R_{O1} at the milliohm level.

The effect of R_{O2} is negligible since it is an additive term to R_2, yielding $\delta R_2 \approx R_{O2}/R_2 < 10^{-8}$.

The resistance R_{O2} is less than 1 Ω, and therefore, the error is less than 10^{-9}.

C. Lead Resistances

The effect of the lead resistances is minimized by the triple connection from the device to the DSB. However, there remains a residual deviation, which was evaluated by means of a Spice circuit simulator according to the methods described in [69]. The effects of the lead resistances connecting the device pads H_1, H_2 and H_3 to the node H and that of the lead resistances connecting the device pads L_1, L_2, and L_3 to L are at the $\delta R_2 \approx 0.1$ nΩ/Ω level and, therefore, negligible. The deviation caused by the resistances R_{lead} of the leads connecting G_1, G_2, and G_3 to node G is shown in Fig. 10. For a measured lead resistance $R_{lead} \approx 3\ \Omega$, $\delta R_2 \approx 1.6\ \mu\Omega/\Omega$, which is nonnegligible with respect to the measurement uncertainty.

D. Stray Resistances

In the present cryogenic setup, there is no guarding circuit and leakage currents can flow through the stray resistances between different terminals. These resistances are represented by R_{HLS}, R_{HGS}, and R_{LGS} in the circuit of Fig. 7. Resistances R_{HGS} and R_{LGS} do not affect the measured value. The resistance R_{HLS} introduces a relative deviation $\delta R_2 \approx R_1/R_{HLS}$ for $R_1 \ll R_{HLS}$. A measurement of the stray resistances yielded values greater than 20 TΩ, limited by the equipment. Therefore, this measurement is only enough to estimate a rough upper bound on the effect of R_{HLS} of $\delta R_2 \approx 50\ \mu\Omega/\Omega$.

E. Drift in the Measured Resistor

The drift of the three resistance standards is approximately 1.5 μΩ/Ω per year for the 100 MΩ resistance standard, 1.6 μΩ/Ω per year for the 1 GΩ standard, and −2.4 μΩ/Ω per year for the 10 GΩ standard. Therefore, over the timescale of these measurements, the drift of those standard resistors is negligible.

VI. Measurement Results

The DSB measurements were performed by directly comparing the graphene 1 GΩ QHARS described in Section II with three resistance standards having nominal values of

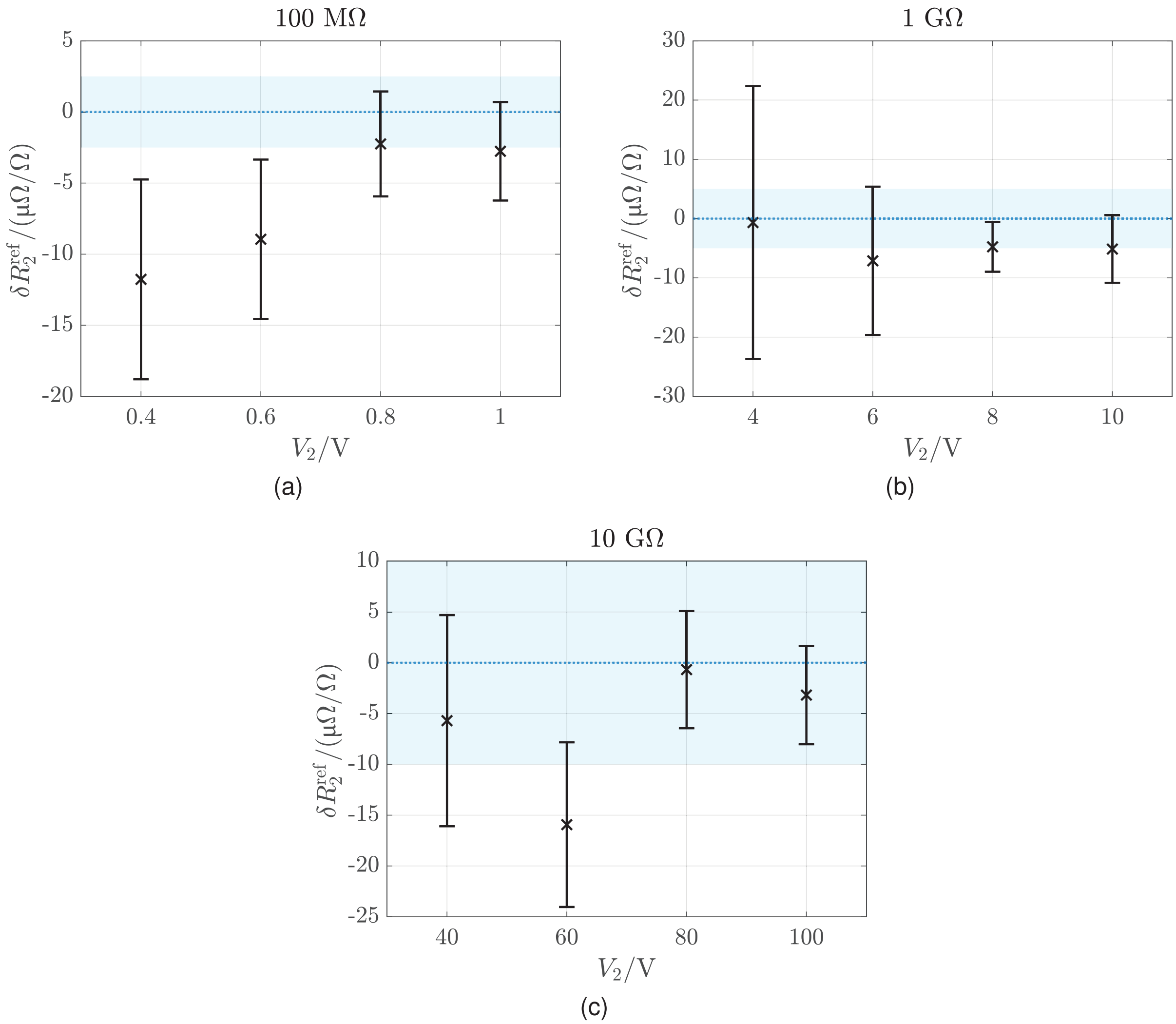

Fig. 11. DSB measurement results at different nominal ratios at selected voltages of (a) customer's 100 MΩ resistor, (b) 1 GΩ standard resistor, and (c) 10 GΩ resistor. The DSB measurement result of the 1 GΩ and 10 GΩ resistor were compared against the predicted value of those standards using the historical calibrated data, while the 100 MΩ measurement was compared with the value obtained from NIST primary scale for high resistance standard. The blue region is the estimated combined standard uncertainty associated with the references, obtained from the historical data trend line and from the primary high resistance range.

100 MΩ, 1 GΩ, and 10 GΩ, corresponding to resistance ratios of approximately 10:1, 1:1, and 1:10, respectively.

For accurate high resistance measurements, high voltages are commonly applied across the resistors to minimize noise and interference, typically above 10 V for a 1 GΩ resistor [56], [58], [59]. However, in this case, applying $V_1 > 10$ V results in a current on the order of I_C, which is the breakdown current of the QHARS. For this reason, the voltages V_1 applied to the QHARS were 4 V, 6 V, 8 V, and 10 V, yielding a reasonable signal-to-noise ratio while remaining below the QHARS I_C. The measurement parameters described in Section IV were: $N = 4$, $M = 100$, $\Delta V_2/V_2 = 5 \times 10^{-2}$, and $K = 2$. All measurements were performed with a detector integration time of 100 power line cycles.

The results, presented in Fig. 11, show the relative deviation $\delta R_2^{\mathrm{ref}} = (\bar{R}_2 - R_2^{\mathrm{ref}})/R_2^{\mathrm{ref}}$ between the measured values $\bar{R}_2$ and the reference resistances R_2^{ref} at different applied nominal voltages $V_2 = -V_1 R_2^{\mathrm{ref}}/R_1$. The values R_2^{ref} are obtained from the NIST primary high resistance range, which is traced to a single quantized Hall resistance standard using a cryogenic current comparator and the NIST primary DSB [8], [56], [58]. The 100 MΩ standard was calibrated before and after the DSB measurements, whereas the values for the 1 GΩ and 10 GΩ standards were obtained by extrapolating the historical calibration data. The uncertainty bars represent the combined standard uncertainties of the DSB measurements against the QHARS, while the blue regions represent the standard uncertainties of R_2^{ref}.

Fig. 12 shows measurements on the 1 GΩ device for voltages above 10 V. The black crosses represent measurements taken with a carrier density of about 1.4×10^{11} cm^{-2}, as in Fig. 11, and the breakdown of the QHE is observed at around 12 V, corresponding to $I_C \approx 127$ μA.

To address this, the carrier density was increased to about 2.8×10^{11} cm^{-2} by annealing the device, as discussed in Section II. The DSB measurements at this higher carrier density are represented by red crosses in Fig. 12. The breakdown of the QHE is observed at around 18 V, from which $I_C \approx 191$ μA. At even higher carrier densities, the breakdown can be raised to above 40 V, corresponding to an $I_C \approx 424$ μA.

TABLE I

PRELIMINARY UNCERTAINTY BUDGET FOR THE MEASUREMENT OF FIG. 11(B), FOR V_2 = 8 V

i	Quantity	x_i		$u(x_i)$	Type	c_i		$u_i(x) = \lvert c_i \rvert u(x_i)$
1	$V_{2,1}^{\mathrm{NULL},+}$	7.306 94	V	0.000 07 V	A	4.8×10^6	Ω/V	0.32 kΩ
2	$V_{2,1}^{\mathrm{NULL},-}$	−7.306 48	V	0.000 21 V	A	-4.8×10^6	Ω/V	1.01 kΩ
3	$V_{2,2}^{\mathrm{NULL},+}$	7.306 44	V	0.000 02 V	A	3.6×10^7	Ω/V	0.59 kΩ
4	$V_{2,2}^{\mathrm{NULL},-}$	−7.307 02	V	0.000 08 V	A	-3.6×10^7	Ω/V	2.78 kΩ
5	$V_{2,3}^{\mathrm{NULL},+}$	7.306 75	V	0.000 03 V	A	2.6×10^7	Ω/V	0.83 kΩ
6	$V_{2,3}^{\mathrm{NULL},-}$	−7.306 21	V	0.000 09 V	A	-2.6×10^7	Ω/V	2.27 kΩ
7	$V_{2,4}^{\mathrm{NULL},+}$	7.306 20	V	0.000 28 V	A	1.8×10^6	Ω/V	0.51 kΩ
8	$V_{2,4}^{\mathrm{NULL},-}$	−7.307 45	V	0.000 23 V	A	-1.8×10^6	Ω/V	0.41 kΩ
9	ΔV_1^+	0	V	0.000 01 V	B	-6.3×10^7	Ω/V	0.73 kΩ
10	ΔV_1^-	0	V	0.000 01 V	B	6.3×10^7	Ω/V	0.73 kΩ
11	ΔV_2^+	0	V	0.000 01 V	B	-6.8×10^7	Ω/V	0.74 kΩ
12	ΔV_2^-	0	V	0.000 01 V	B	6.8×10^7	Ω/V	0.74 kΩ
13	$R_{\mathrm{lead},1}$	3.0	Ω	0.29 Ω	B	5.3×10^1	Ω/Ω	0.15 kΩ
14	$R_{\mathrm{lead},2}$	3.0	Ω	0.29 Ω	B	5.3×10^1	Ω/Ω	0.15 kΩ
15	$R_{\mathrm{lead},3}$	3.0	Ω	0.29 Ω	B	5.3×10^1	Ω/Ω	0.15 kΩ
	$\bar{R}_2$	1.000 158 9 GΩ			RSS			4.2 kΩ [3.6 μΩ/Ω]

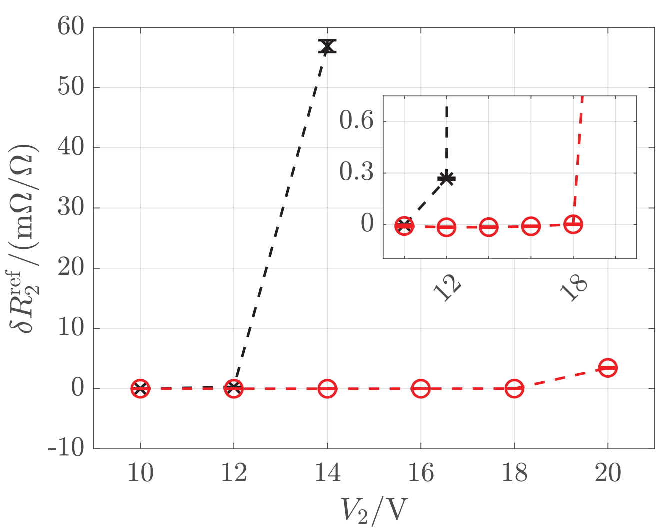

Fig. 12. Breakdown of the QHE observed in the 1 GΩ QHARS occurred at high applied voltages, corresponding to high current bias conditions. The critical current I_C increased with the increment of carrier density n_e (represented by red circles), compared to the lower values observed initially (indicated by black crosses).

The uncertainty budget for the 1 GΩ resistance standard against the graphene QHARS DSB measurement was estimated according to [63]. The measurement was performed at 8 V. The first contributions are the type A uncertainties, at each polarity, of the nanovoltmeter readings for each interpolated balanced values of $V_{2,l}^{\mathrm{NULL},\pm}$. These uncertainties are evaluated and reported in the first eight rows in Table I.

The contributions from rows 9 to 12 are associated with the two calibrators, in which the output voltage errors are evaluated according to the specifications of the instruments [67], [68].

Rows 13–15 are the corrections for the ground lead resistances, which is another significant contribution. This value depends on the wiring inside the cryostat probe and is difficult to reduce even with the triple connection implemented on the QHARS.

The stray resistance R_{HLS} effect, on the other hand, requires more careful investigation to precisely estimate its contribution to the final result.

VII. CONCLUSION

This work demonstrates the feasibility of utilizing a star-mesh QHARS device to generate a 1 GΩ quantized resistance standard. By combining this novel device with a DSB, a robust foundation for a primary resistance standard at the 1 GΩ level was established. This approach has the potential to significantly enhance the accuracy and efficiency of high resistance measurements by replacing lengthy calibration chains of multiple resistance standards and bridges used when scaling from the i = 2 quantum Hall value of 12906.4037...Ω to the MΩ, GΩ, and TΩ resistance ranges. The removal of 5–8 decades of transfer resistance standards in high resistance scaling is an attractive proposition, bringing quantized Hall resistance standards directly to high resistance ranges. Compared to traditional room-temperature standards, the quantized resistance value automatically guarantees stability over time, temperature, and humidity.

QHARS devices, using the star-mesh network beyond 1 GΩ, will use far fewer elements than series arrays but present additional challenges such as considerations in the wiring of probes and choice of materials to suppress stray resistances and leakage currents which can introduce errors to the measurement system. Moreover, a DSB operated with star-mesh networks has reduced sensitivity and increased current noise with respect to one operated with series arrays. The reduced sensitivity is due both to the lower maximum applicable voltage, constrained by the lower resistance seen by the voltage source, and to the low equivalent resistance in parallel to the detector. These limitations also occur with traditional room-temperature Y-standards. As a consequence, the measurement uncertainties so far obtained in this work are of the same order of magnitude as those derived from historical trends, which are generally based on measurements performed by applying up to 100 V. The voltage limitation can be overcome with an asymmetric QHARS design, increasing the resistance seen by the voltage source, allowing to obtain higher sensitivities.

Finally, an important open problem concerning QHARS is the verification of the QHE elements' full quantization. Indeed, a way to verify the full quantization of all individual QHE elements in a QHARS has not been found yet. In this work, the quality of the monolayer graphene was determined by optical and confocal scanning microscopy and the QHARS quantization was assessed by magnetotransport measurements of R_{HL} and of the R_{xx} at accessible terminals. R_{HL} was found to agree with the calculated value of the 37 element QHARS. Moreover, the chosen magnetic field strength is sufficiently high to allow the quantization of all elements even with doping inhomogeneities within the device.

Disclaimer

Commercial equipment identified in this article does not imply recommendation or endorsement by the National Institute of Standards and Technology (NIST), Gaithersburg, MD, USA, nor does it imply that the identified equipment is the best for the purpose.

References

[1] A. K. Geim and K. S. Novoselov, "The rise of graphene," *Nature Mater.*, vol. 6, no. 3, pp. 183–191, Mar. 2007.

[2] F. Guinea, N. M. R. Peres, K. S. Novoselov, and A. K. Geim, "The electronic properties of graphene," *Rev. Mod. Phys.*, vol. 81, no. 1, pp. 109–162, 2009.

[3] S. Adam, E. H. Hwang, and E. Rossi, "Electronic transport in two-dimensional graphene," *Rev. Modern Phys.*, vol. 83, no. 2, pp. 407–470, May 2011.

[4] V. I. Fal'ko, L. Colombo, P. R. Gellert, M. G. Schwab, and K. Kim, "A roadmap for graphene," *Nature*, vol. 490, pp. 192–200, Oct. 2012.

[5] B. Jeckelmann and B. Jeanneret, "The quantum Hall effect as an electrical resistance standard," *Rep. Prog. Phys.*, vol. 64, no. 12, p. 1603, 2001.

[6] A. F. Rigosi and R. E. Elmquist, "The quantum Hall effect in the era of the new Si," *Semiconductor Sci. Technol.*, vol. 34, no. 9, Sep. 2019, Art. no. 093004.

[7] R. Ribeiro-Palau et al., "Quantum Hall resistance standard in graphene devices under relaxed experimental conditions," *Nature Nanotechnol.*, vol. 10, no. 11, pp. 965–971, Nov. 2015.

[8] T. Oe et al., "Comparison between NIST graphene and AIST GaAs quantized Hall devices," *IEEE Trans. Instrum. Meas.*, vol. 69, no. 6, pp. 3103–3108, Jun. 2020.

[9] A. Tzalenchuk et al., "Towards a quantum resistance standard based on epitaxial graphene," *Nature Nanotechnol.*, vol. 5, no. 3, pp. 186–189, Mar. 2010.

[10] H. He et al., "Stable and tunable charge carrier control of graphene for quantum resistance metrology," in *Proc. Conf. Precis. Electromagn. Meas. (CPEM)*, Jul. 2018, pp. 1–2.

[11] T. J. B. M. Janssen et al., "Anomalously strong pinning of the filling factor *ν=2* in epitaxial graphene," *Phys. Rev. B, Condens. Matter*, vol. 83, no. 23, Jun. 2011, Art. no. 233402.

[12] A. F. Rigosi et al., "Graphene devices for tabletop and high-current quantized Hall resistance standards," *IEEE Trans. Instrum. Meas.*, vol. 68, no. 6, pp. 1870–1878, Jun. 2019.

[13] M. Kruskopf et al., "Graphene quantum Hall effect devices for AC and DC electrical metrology," *IEEE Trans. Electron Devices*, vol. 68, no. 7, pp. 3672–3677, Jul. 2021.

[14] M. Marzano et al., "Implementation of a graphene quantum Hall Kelvin bridge-on-a-chip for resistance calibrations," *Metrologia*, vol. 57, no. 1, Jan. 2020, Art. no. 015007.

[15] F. Delahaye, "Series and parallel connection of multiterminal quantum Hall-effect devices," *J. Appl. Phys.*, vol. 73, no. 11, pp. 7914–7920, Jun. 1993.

[16] K. Matsuhiro, T. Itatani, S. Gorwadkar, S. Kiryu, and N.-H. Kaneko, "New design of quantized Hall resistance array device," *IEEE Trans. Instrum. Meas.*, vol. 62, no. 6, pp. 1755–1759, Jun. 2013.

[17] S. Lara-Avila, A. Danilov, S. Kubatkin, A. Tzalenchuk, and R. Yakimova, "A prototype of RK/200 quantum Hall array resistance standard on epitaxial graphene," *J. Appl. Phys.*, vol. 118, no. 4, Jul. 2015, Art. no. 044506.

[18] S. Novikov et al., "Mini array of quantum Hall devices based on epitaxial graphene," *J. Appl. Phys.*, vol. 119, no. 17, May 2016, Art. no. 174504.

[19] W.-S. Kim, and D.-H. Chae, "Realization of $5\frac{h}{e^2}$ with graphene quantum Hall resistance array," *Appl. Phys. Lett.*, vol. 116, no. 9, Mar. 2020, Art. no. 093102.

[20] M.-S. Kim, T. Oe, and N.-H. Kaneko, "Series connection of quantum Hall resistance array and programmable Josephson voltage standard for current generation at one microampere," *Metrologia*, vol. 59, no. 6, Nov. 2022, Art. no. 065011.

[21] S. M. Mhatre et al., "Versatility of uniformly doped graphene quantum Hall arrays in series," *AIP Adv.*, vol. 12, no. 8, Aug. 2022, Art. no. 085113.

[22] H. He et al., "Accurate graphene quantum Hall arrays for the new international system of units," *Nature Commun.*, vol. 13, no. 1, p. 6933, Nov. 2022.

[23] D. G. Jarrett et al., "Graphene-based star-mesh resistance networks," *IEEE Trans. Instrum. Meas.*, vol. 72, pp. 1–10, 2023.

[24] M. Abrate, and L. Callegaro, "On the synthesis of quantum Hall array resistance standards," *Metrologia*, vol. 52, no. 1, pp. 31–39, Feb. 2015.

[25] S. Gorwadkar, T. Itatani, and N.-H. Kaneko, "Development of 1Ω quantum Hall array resistance standards," *IEEE Trans. Instrum. Meas.*, vol. 66, pp. 1475–1481, 2017.

[26] J. Hu et al., "Towards epitaxial graphene p–n junctions as electrically programmable quantum resistance standards," *Sci. Rep.*, vol. 8, no. 1, p. 15018, Oct. 2018.

[27] M. Friedemann, T. Dziomba, T. Weimann, and F. J. Ahlers, "Graphene p-n junction arrays as quantum-Hall resistance standards," *Appl. Phys. Lett.*, vol. 99, no. 2, Jul. 2011, Art. no. 022112.

[28] D. Patel et al., "Accessing ratios of quantized resistances in graphene p–n junction devices using multiple terminals," *AIP Adv.*, vol. 10, no. 2, Feb. 2020, Art. no. 025112.

[29] S. Heun, G. Biasiol, and S. Roddaro, "Cascaded quantum Hall bisection and applications to quantum metrology," *Phys. Rev. Appl.*, vol. 14, no. 2, Aug. 2020, Art. no. 024059.

[30] A. F. Rigosi et al., "Analytical determination of atypical quantized resistances in graphene p-n junctions," *Phys. B, Condens. Matter*, vol. 582, Apr. 2020, Art. no. 411971.

[31] M. Kruskopf et al., "Next-generation crossover-free quantum Hall arrays with superconducting interconnections," *Metrologia*, vol. 56, no. 6, Dec. 2019, Art. no. 065002.

[32] D. G. Jarrett, A. F. Rigosi, S. U. Payagala, and M. E. Kraft, "Comparison of multiple methods for obtaining PΩ resistances with low uncertainties," *IEEE Trans. Instrum. Meas.*, vol. 69, no. 6, pp. 3729–3738, Jun. 2020.

[33] D. S. Scaletta et al., "Optimization of graphene-based quantum Hall arrays for recursive star–mesh transformations," *Appl. Phys. Lett.*, vol. 123, no. 15, Oct. 2023, Art. no. 153504.

[34] H. A. Sauer, "Wye-delta transfer standards for calibration of wide range DC resistance and DC conductance bridges," *IEEE Trans. Instrum. Meas.*, vol. IM-17, no. 2, pp. 151–155, Nov. 1968.

[35] K. Küpfmüller, *Einfuhrung in Die Theoretische Elektrotechnik*. Berlin, Germany: Springer, 1959.

[36] R. E. Scott, *Linear Circuits*. Reading, MA, USA: Addison-Wesley, 1960.

[37] L. Callegaro, *Electrical Impedance: Principles, Measurement, and Applications*. Boca Raton, FL, USA: CRC Press, 2013.

[38] A. E. Kennelly, "The equivalence of triangles and three-pointed stars in conducting networks," *Electr. World Engineer*, vol. 34, no. 12, pp. 413–414, Sep. 1899.

[39] Y. Semenov and I. Samodurov, "Microwire-wound resistors in high value resistance measurements in VNIIM," in *Proc. CPEM*, Jun. 2010, pp. 643–644.

[40] J. H. Kang, S. H. Lee, S. J. Joo, and H.-K. Lee, "Development of wye-delta-type high-resistance standards in the range of 1 mΩ to 1 GΩ," *J. Electr. Eng. Technol.*, vol. 17, pp. 1987–1992, Apr. 2022.

[41] L. Versfeld, "Remarks on star-mesh transformation of electrical networks," *Electron. Lett.*, vol. 6, no. 19, pp. 597–599, Sep. 1970.

[42] S. Seshu and N. Balabanian, *Linear Network Analysis*. Hoboken, NJ, USA: Wiley, 1959.
[43] A. Morgan-Voyce, “Ladder-network analysis using Fibonacci numbers,” *IRE Trans. Circuit Theory*, vol. 6, no. 3, pp. 321–322, Sep. 1959.
[44] V. Mowery, “Fibonacci numbers and tchebycheff polynomials in ladder networks,” *IRE Trans. Circuit Theory*, vol. 8, no. 2, pp. 167–168, 1961.
[45] R. Buring, “Formulas for the terminal impedances and transfer functions of general multimesh ladder networks,” *Proc. IEEE*, vol. 53, no. 7, pp. 736–737, Jul. 1965.
[46] M. Kruskopf et al., “Comeback of epitaxial graphene for electronics: Large-area growth of bilayer-free graphene on SiC,” *2D Mater.*, vol. 3, no. 4, Sep. 2016, Art. no. 041002.
[47] A. R. Panna et al., “Graphene quantum Hall effect parallel resistance arrays,” *Phys. Rev. B, Condens. Matter*, vol. 103, no. 7, Feb. 2021, Art. no. 075408.
[48] V. Panchal et al., “Confocal laser scanning microscopy for rapid optical characterization of graphene,” *Commun. Phys.*, vol. 1, no. 1, p. 83, Nov. 2018.
[49] M. Kruskopf et al., “Two-terminal and multi-terminal designs for next-generation quantized Hall resistance standards: Contact material and geometry,” *IEEE Trans. Electron Devices*, vol. 66, no. 9, pp. 3973–3977, Sep. 2019.
[50] R. Elmquist, and M. Cage, “Precision tests of a quantum Hall effect device DC equivalent circuit using double-series and triple-series connections,” *J. Res. Natl. Inst. Stand. Technol.*, vol. 100, no. 6, pp. 677–685, 1995.
[51] S. M. Mhatre et al., “Dynamics of transient hole doping in epitaxial graphene,” *Phys. Rev. B, Condens. Matter*, vol. 105, no. 20, May 2022, Art. no. 205423.
[52] Y. Yang, S. Pookpanratana, C. A. Hacker, C.-T. Liang, and R. E. Elmquist, “Chemical-doping-driven crossover from graphene to ‘ordinary metal,”’ *Nanoscale*, vol. 9, no. 32, pp. 11537–11544, Aug. 2017.
[53] P. Streda, “Breakdown of the quantum Hall effect,” *J. Phys. C, Solid State Phys.*, vol. 19, no. 7, pp. L155–L159, Mar. 1986.
[54] T. J. B. M. Janssen et al., “Operation of graphene quantum Hall resistance standard in a cryogen-free table-top system,” *2D Mater.*, vol. 2, no. 3, Aug. 2015, Art. no. 035015.
[55] J. A. Alexander-Webber et al., “Phase space for the breakdown of the quantum Hall effect in epitaxial graphene,” *Phys. Rev. Lett.*, vol. 111, no. 9, Aug. 2013, Art. no. 096601.
[56] S. U. Payagala, M. E. Kraft, and K. M. Yu, “Third generation of adapted Wheatstone bridge for high resistance measurements at NIST,” in *Proc. Conf. Precis. Electromagn. Meas. (CPEM)*, Jul. 2016, pp. 1–2.
[57] G. Rietveld and J. H. N. van der Beek, “Automated high-ohmic resistance bridge with voltage and current null detection,” *IEEE Trans. Instrum. Meas.*, vol. 62, no. 6, pp. 1760–1765, Jun. 2013.
[58] S. Payagala, A. R. Panna, S. Takada, N.-H. Kaneko, and D. G. Jarrett, “Precise high resistance comparison between the NMIJ traveling dual source bridge and the NIST adapted wheatstone bridge,” *Metrologia*, vol. 59, no. 6, Dec. 2022, Art. no. 065007.
[59] L. C. A. Henderson, “A new technique for the automatic measurement of high value resistors,” *J. Phys. E, Sci. Instrum.*, vol. 20, no. 5, pp. 492–495, May 1987.
[60] R. D. Cutkosky, “A new switching technique for binary resistive dividers,” *IEEE Trans. Instrum. Meas.*, vol. IM-27, no. 4, pp. 421–422, Apr. 1978.
[61] S. H. Tsao, “A 25-bit reference resistive voltage divider,” *IEEE Trans. Instrum. Meas.*, vols. IM-36, no. 2, pp. 285–290, Jun. 1987.
[62] J. Millman, “A useful network theorem,” *Proc. IRE*, vol. 28, no. 9, pp. 413–417, Sep. 1940.
[63] *Evaluation of Measurement Data—Guide to the Expression of Uncertainty in Measurement*, BIPM, IEC, IFCC, ILAC, ISO, IUPAC, IUPAP, and OIML, 2008.
[64] H. Toutenburg, Shalabh, and C. Heumann, *Linear Models and Generalizations*, 3rd ed., Berlin, Germany: Springer, 2008.
[65] Evaluation of Measurement Data—Supplement 2 to the ‘Guide to the Expression of Uncertainty in Measurement’—Extension to any Number of Output Quantities, Standard JCGM 102:2011, BIPM, IEC, IFCC, ILAC, ISO, IUPAC, IUPAP, and OIML, pp. –2011.
[66] J. Hoffmann, and M. Wollensack, “Metas.UncLib—A measurement uncertainty calculator for advanced problems,” *Metrologia*, vol. 49, no. 6, pp. 809–815, Nov. 2012.
[67] *Series II Multi-function Calibrator Operators Manual*, document 5700A/5720A, Fluke Corporation, 2002.
[68] *Multi-function Calibrator Operators Manual*, document 5730A, Fluke Corporation, 2023.
[69] M. Ortolano and L. Callegaro, “Circuit models and SPICE macro-models for quantum Hall effect devices,” *Meas. Sci. Technol.*, vol. 26, no. 8, Aug. 2015, Art. no. 085018.

Marta Musso was born in Turin, Italy, in 2000. She received the B.Sc. and M.Sc. degrees in electronic engineering from the Politecnico di Torino, Turin, in 2022 and 2024, respectively, where she is currently pursuing the Ph.D. degree in electrical, electronic and communications engineering.

In 2024, she spent six months as a Guest Researcher at the National Institute of Standards and Technology (NIST), Gaithersburg, MD, USA. Her research interests are in electrical quantum metrology, specifically on the use of quantum Hall effect devices in impedance and low current metrology.

Wei-Chen Lin was born in New Taipei City, Taiwan, in 1996. He received the B.S. degree in physics from National Chung Hsing University, Taichung, Taiwan, in 2019. He is currently pursuing the Ph.D. degree with Prof. Chi-Te Liang’s Laboratory, National Taiwan University (NTU), Taipei, Taiwan.

Since 2024, he has been with the National Institute of Standards and Technology (NIST), Gaithersburg, MD, USA, as a Guest Researcher, for a year. His research focuses on low-temperature transport measurements in topological materials, superconductors, and transition metal dichalcogenides.

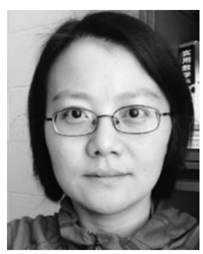

Yanfei Yang received the B.S. degree in applied optics from Sichuan University, Chengdu, China, in 1999, and the Ph.D. degree in physics from Georgetown University, Washington, DC, USA, in 2010. Her Ph.D. thesis was focused on quantum transport in carbon nanotubes and the investigation of possible intrinsic superconductivity in isolated carbon nanotubes.

Since 2012, she has been a Researcher with the National Institute of Standards and Technology (NIST), Gaithersburg, MD, USA, where she has been involved in the development of new resistance standards based on quantum Hall devices made of epitaxial graphene.

Dr. Yang was awarded the Physical Measurement Laboratory’s (NIST) Distinguished Associated Award for advancing quantum metrology through the development of graphene quantum Hall resistance standards that offer robust, accurate, and cost-effective dissemination of the ohm.

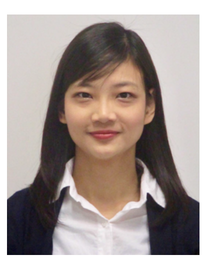

Ngoc Thanh Mai Tran was born in Ho Chi Minh City, Vietnam, in 1992. She received the B.Sc. and M.Sc. degrees in electronic engineering from the Politecnico di Torino, Turin, Italy, in 2014 and 2017, respectively, and the Ph.D. degree in metrology from the Politecnico di Torino and the Istituto Nazionale di Ricerca Metrologica, Turin, in 2021.

In 2016, she did her master’s thesis at the National Metrology Institute of Japan (NMIJ), Tsukuba, Japan. From 2019 to 2020, she was a Guest Researcher with Korea Research Institute of Standards and Science (KRISS), Daejeon, South Korea. She is currently an Assistant Research Scientist Associate with the Joint Quantum Institute (JQI), University of Maryland, College Park, MD, USA, and the National Institute of Standards and Technology (NIST), Gaithersburg, MD, USA. She is involved in several projects related to the metrology of electrical resistance and impedance.

Alireza R. Panna was born in Mumbai, India. He received the B.S. degree in electrical engineering from the University of Maryland, College Park, MD, USA, in 2013.

From 2012 to 2013, he worked as a Guest Researcher with the National Institute of Standards and Technology (NIST), Gaithersburg, MD, USA, where he was involved in magnet characterization for the NIST-4 watt balance. From 2013 to 2017, he was with the National Institutes of Health, Bethesda, MD, USA, where he worked on controls and characterization of various X-ray imaging modalities. He is currently with NIST, where he is involved in the Metrology of the Ohm and the Quantum Conductance Projects.

Cheng-Hsueh Yang received the master's degree from National Kaohsiung Normal University (NKNU), Kaohsiung, Taiwan, in 2019. He is currently pursuing the Ph.D. degree with National Taiwan University (NTU), Taipei, Taiwan.

He was a Research Assistant with National Cheng Kung University (NCKU), Tainan, Taiwan, from 2019 to 2020. From 2023 to 2024, he was a Guest Researcher with the National Institute of Standards and Technology (NIST), Gaithersburg, MD, USA. His research focuses on low-temperature transport measurements of 2-D materials, with additional projects exploring quantum dot spin qubits.

Randolph E. Elmquist (Senior Member, IEEE) received the Ph.D. degree in physics from the University of Virginia, Charlottesville, VA, USA, in 1986.

He leads the Quantum Conductance Project at the National Institute of Standards and Technology (NIST), Gaithersburg, MD, USA. Working for the past 32 years in the field of electrical and quantum metrology, he has contributed to the experimental design and measurement of the electronic kilogram and calculable impedance standards for the determination of the von Klitzing constant and alpha, the unitless fine structure constant. He led the development of cryogenic current comparator systems, the quantum Hall effect, and graphene electronic devices for metrology. After 38 years of service to NIST, Rand Elmquist retired in 2024.

Dr. Elmquist is a member of American Physical Society.

David B. Newell received the B.S. degree in physics and the B.A. degree in mathematics from the University of Washington, Seattle, WA, USA, and the Ph.D. degree in physics from the University of Colorado, Boulder, Colorado.

He was awarded the NRC Postdoctoral Fellowship to work on the Watt Balance Project at the National Institute of Standards and Technology (NIST), Gaithersburg, MD, USA, where he became a full-time Staff Member in 1996. He has worked on measurements for realizing microscale and nanoscale forces traceable to the SI, was the Leader of the Fundamental Electrical Measurements (FEM) Group from 2004 to 2010, helped to establish the use of graphene in quantum electrical standards, worked with the NIST Team to construct a new watt balance to realize the kilogram from a fixed value of the Planck constant, and as the Chair of the CODATA Task Group on Fundamental Constants, provided the exact values of the fundamental constants to be used in the new SI. He has presently again accepted responsibility as the Leader of the FEM Group.

Dr. Newell is a member of the Philosophical Society of Washington, the Chair of the CODATA Task Group on Fundamental Constants, and a fellow of American Physical Society.

Chi-Te Liang was born in Taipei, Taiwan, in 1968. He received the B.S. degree in physics from National Taiwan University, Taipei, in 1990, and the Ph.D. degree from Cambridge University, Cambridge, U.K., in 1996.

He served in Marine Corps, Taichung, Taiwan, from 1990 to 1992. He did his post-doctoral work at Cambridge University from 1996 to 1999. Since 1999, he has been with the Department of Physics, National Taiwan University. He has been working on quantum transport in low-dimensional systems.

Prof. Liang was elected as a fellow of the Institute of Physics (IOP), U.K., in 2014, and the Physical Society of Taiwan (TPS) in 2024.

Massimo Ortolano was born in 1969. He received the M.Sc. degree in electronic engineering and the Ph.D. degree in metrology from the Politecnico di Torino, Turin, Italy, in 1997 and 2001, respectively.

Since 2000, he has been with the Department of Electronics and Telecommunications, Politecnico di Torino, where he is currently an Associate Professor. He teaches classes about electronic measurements and sensors. Since 2006, he has been collaborating with the Istituto Nazionale di Ricerca Metrologica (INRIM), Turin, with a focus on noise metrology, modeling of quantum Hall effect devices, and impedance metrology, and he has been a Visiting Researcher at several national metrology institutes worldwide. His research interests include low current measurements, fundamental constants, time and frequency metrology, and statistical methods for the evaluation of uncertainty.

Albert F. Rigosi (Member, IEEE) was born in New York, NY, USA. He received the B.A., M.A., M.Phil., and Ph.D. degrees in physics from Columbia University, New York.

From 2008 to 2015, he was a Research Assistant with the Columbia Nano Initiative, New York. From 2015 to 2016, he was a Joint Visiting Research Scholar with the Department of Applied Physics, Stanford University, Stanford, CA, USA, and the PULSE Institute of SLAC National Accelerator Laboratory, Menlo Park, CA, USA. Since 2016, he has been a Physicist with the National Institute of Standards and Technology, Gaithersburg, MD, USA. His research interests include 2-D electron systems and applications of those systems' behaviors for electrical metrology.

Dr. Rigosi is a member of American Physical Society and the Advisory Board for the Industrial Leadership in Physics Ph.D. Program at Georgetown University. He was awarded associateships and fellowships from the National Research Council, USA, the Optical Society of America, the Ford Foundation, and the National Science Foundation (Graduate Research Fellowship Program).

Dean G. Jarrett (Fellow, IEEE) was born in Baltimore, MD, USA, in 1967. He received the B.S. degree in electrical engineering from the University of Maryland, College Park, MD, USA, in 1990, and the M.S. degrees in electrical engineering and applied biomedical engineering from Johns Hopkins University, Baltimore, MD, USA, in 1995 and 2008, respectively.

Since 1986, he has been with the National Institute of Standards and Technology (NIST), Gaithersburg, MD, USA, where he was a Cooperative Education Student with the University of Maryland. During this time, he worked in the dc resistance area on the automation of resistance calibration systems. In 1991, he joined NIST, as a full-time Electrical Engineer, working on the development of an automated ac resistance calibration system and the development of new resistance standards. Since 1994, he has been working in the high-resistance laboratory developing automated measurement systems and improving standard resistors to support high-resistance calibration services and key comparisons. In recent years, he has worked on sensor technologies for the detection of biological molecules and low-current source and measure techniques. Since 2014, he has been leading the Metrology of the Ohm Project at NIST.